PNAS
www.pnas.org

Supplementary Information for

Hierarchical dynamics as a macroscopic organizing principle of the human brain

Ryan V. Raut, Abraham Z. Snyder, & Marcus E. Raichle

Ryan V. Raut
Email: raut@wustl.edu

This PDF file includes:

Supplementary Text
Supplementary Methods
Figures S1 to S6
SI References

www.pnas.org/cgi/doi/10.1073/pnas.2003383117

Supplementary Text

Quantifying extensive functional connectivity

At present, there is no standard practice for measuring the strength of functional connectivity (FC) [1]. The present study uses global signal regression (GSR) for denoising [2] and to enhance spatial specificity. This maneuver essentially zero-centers the correlation distribution [3]. FC (positive or negative) reflects the extent to which a signal observed in one region shares variance with signals in other regions. Furthermore, the strongest anti-correlations manifest between large-scale allocentric and egocentric systems (traditionally, "task-positive" and "task-negative," respectively) [3, 4]. The antagonistic relationship between these systems is a significant feature of brain functional organization [5-8] and, hence, warrants consideration. Accordingly, we defined FC strength as mean absolute value correlation (Figs. 4 & S4A).

Alternatively, we may compute the unweighted (i.e., binary) graph metric of FC degree [9]. This metric reports the number of correlations exceeding some (arbitrary) threshold. Following a prior investigation of the relationship between fMRI spectral content and FC topology [10], we computed FC degree as the number of pairwise correlations > +0.3. Similar to absolute value FC strength (Fig. S4A), FC degree indicated strongly positive associations with intrinsic timescale, with significant individual-specificity (within- vs. between-subject ACF decay:FC degree $p < .001$) (Fig. S4B). Thus, our major intrinsic timescale:FC results (Fig. 4) are also obtained by analyzing only the strongest positive correlations.

Crucially, both absolute value FC strength and FC degree indicate that association cortex exhibits the most extensive FC, which is predicted from structural connectivity at micro- and macro-structural scales [12]. Moreover, the observed timescale:FC relationship agrees with prior work that has modeled and/or observed an association between slow timescales and extensive FC [10, 11]. A similar phenomenon appears to manifest at a cellular scale [13, 14]. An intuitive explanation for this fundamental relationship is that the summation of inputs to a cell or region has the effect of a low-pass filter, to an extent that depends on the number of inputs (i.e., extent of connectivity) [10].

One may also consider measuring the strength of FC by computing mean signed (i.e., non-absolute value) FC. However, following GSR, the approximately equal number of positive and negative correlations complicates treatment of FC as a signed quantity when computing mean FC. Computing mean signed FC in our global signal-regressed data, we observe overall weak and negative correlations between FC strength and intrinsic timescale, and non-significant individual specificity ($p = .26$) (Fig. S4C). The strong dependence of mean signed FC on use of GSR has been demonstrated previously [15] (see also the section entitled "Considerations for Using Global Brain Connectivity (GBC)" in the Supplementary Appendix of [16]).

A recent study computed mean signed FC – referred to as "global brain connectivity (GBC)" – in non-GSR fMRI data [17]. GBC was found to be highest in sensorimotor regions and weakest in multimodal association areas. The initial study to employ the GBC measure (also without GSR) [18] observed a cortical topography that more closely aligns with the conventional view of increased functional and structural connectivity in association areas [19]. It is possible that these discrepancies result from other preprocessing steps, e.g., low-pass filtering (used in [18]).

Supplementary Methods

fMRI processing

Functional data were preprocessed to reduce artifact, maximize cross-session registration, and resample to an atlas space. For each MSC subject a mean of field maps collected over multiple sessions was applied to images from all sessions for distortion correction, as described in detail elsewhere [20]. All scans underwent correction for odd-even slice intensity differences stemming from interleaved acquisition of slices within a volume, correction for within-volume slice-dependent time shifts, intensity normalization to a whole brain mode value of 1000, and within- and between-run rigid body correction for head movement. Transformation to Talairach atlas space [21] was computed by registering the mean intensity image from a single BOLD session via the average T1-weighted image and average T2-weighted image, and subsequent BOLD sessions were linearly aligned to this first session. This atlas transformation was combined with mean field distortion correction and resampling to 3 mm isotropic atlas space in a single step.

Atlas-transformed, volumetric time series were further processed to reduce artifact. First, temporal masks were created to flag motion-contaminated frames. Such frames were identified by outlying values of framewise displacement (FD), a scalar index of instantaneous head motion, computed as the sum of the magnitudes of the differentiated translational (three) and rotational (three) motion parameters [22]. Several MSC subjects exhibited power spectral peaks at the respiratory frequency especially in the phase-encoding direction (y; anterior-to-posterior) [23]. Because this oscillatory artifact did not obviously corrupt the data and occurred above frequencies of interest (>0.1 Hz), we low-pass filtered the *y*-motion time course at 0.1 Hz in all MSC subjects prior to computing FD to prevent inflation of FD values and superfluous data loss [24, 25]. Frames with FD exceeding 0.5 mm were replaced by linear interpolation to yield continuous time series that could be filtered while mitigating the spread of motion artifact to surrounding frames [26]. Interpolated BOLD time series, as well as motion parameters [27] were next passed through a zero-phase second-order Butterworth low-pass filter (f < 0.1 Hz) to mitigate high-frequency artifact.

Next, the filtered BOLD time series underwent nuisance regression. For GSP subjects, an atlas white matter and ventricle mask were treated as nuisance compartments and the mean and first derivative of signals from these regions and from the whole brain (global signal), as well as the filtered six realignment estimates, were regressed from the filtered time series. For the MSC subjects, filtered time series underwent regression of the global signal as well as principal components derived from subject-specific masks of white matter and ventricles (segmented via FreeSurfer [28, 29]) and extra-axial space [30] (as defined by a thresholded temporal standard deviation image), and from the six filtered motion parameters. Component-based regression of MSC data is described in detail elsewhere [31]. Interpolated time points were re-censored using a temporal mask for all analyses, except where continuous time series were required (i.e., generating power spectra (Fig. S1) and the spectral normalization control analysis (see *Comparison with functional connectivity* in main text Methods)).

Processed time series were transformed to MNI152 space prior to surface mapping. For each subject, the atlas-transformed T1-weighted image was nonlinearly warped to the MNI152 template using FSL's FNIRT [32] and the resulting transform was applied to BOLD runs.

Generation of individual cortical surfaces for MSC dataset

As described previously [23], each MSC subject's anatomical surface was generated from their average T1-weighted image in native volumetric space using FreeSurfer's "recon-all" processing pipeline. The pipeline entailed brain extraction and segmentation (hand-edited for accuracy), generation of white matter and pial surfaces, inflation of surfaces to a sphere, and spherical registration of the original surface to the "fsaverage" [28, 33-37]. The fsaverage-registered left and right hemispheres were placed in correspondence with one another by applying deformation maps from a landmark-based registration of left and right fsaverage surfaces to a hybrid left-right fsaverage surface ('fs_LR') ([38]). These deformation maps were combined with those for resampling to a resolution of 164,000 vertices per hemisphere (164k fs_LR) and downsampling to a resolution of ~4,000 vertices per hemisphere ('4k fs_LR'). These various surfaces in native volumetric space were then transformed to MNI152 atlas volumetric space using Caret tools [39].

Surface processing and CIFTI creation

Processed BOLD time series were converted to CIFTI format, which projects data from cortical voxels to a surface while retaining volumetric time series from the subcortex and cerebellum [40]. CIFTI creation proceeded as follows: BOLD time series from each subject were sampled to their native mid-thickness surfaces (created by averaging the white and pial surfaces) using the "ribbon-constrained" sampling procedure [41] from Connectome Workbench. Once sampled to the native surface, time courses were deformed and resampled from the individual's original surface to a ~4,000 vertex (per hemisphere) fs_LR surface in a single step using the deformation map generated above. GSP volume data were sampled directly to the Conte69 atlas mid-thickness surface using the ribbon-constrained sampling procedure and subsequently downsampled to the 4k fs_LR surface. Downsampling to ~6 mm spacing was performed to improve SNR and reduce computational demand. Surface time series were subsequently geodesically smoothed along the respective subject's (or for GSP, the atlas) cortical surface, as described in Glasser et al. [41], with a 2D Gaussian kernel ($\sigma = 4.25$). For display purposes only, spectral maps were upsampled to ~32k, ~2 mm resolution surfaces and geodesically smoothed ($\sigma = 1.70$). All (surface) computations were performed at 6 mm resolution.

Surface time series were combined with volumetric subcortical data into the CIFTI format using Connectome Workbench [40], creating full brain time courses excluding non-gray matter tissue. Volumetric time series were smoothed using a structure-constrained procedure [41] ($\sigma = 2.55$) following nonlinear alignment to the MNI152 atlas.

Network parcellation

Cortical, striatal, and cerebellar parcellations were obtained from Buckner et al. [42-44] and resampled to the 4k surface (cortex) or 3 mm resolution (subcortex). Low SNR regions in medial prefrontal cortex and anterior and ventral portions of the temporal lobe [45] were excluded (gray regions in Fig. 1B; 461/7,320 total cortical vertices), as previously (e.g., [20]), on the basis of a mean signal map. The limbic network was excluded from analysis due to its overlap with low SNR regions in cortex [42] and striatum [44], and with white matter in the cerebellum [43]. The

visual network in the cerebellum and visual and dorsal attention networks in the striatum were also omitted from the present analyses as little-to-no representation of these networks has been identified in these structures on the basis of FC [43, 44, 46, 47]. The above criteria retained 6,398/7,320 (87.4%) of cortical vertices, 911/988 (91.0%) of striatal gray matter voxels, and 5,403/5,669 (95.3%) of cerebellar gray matter voxels. To generate a comparable parcellation for the thalamus, we applied a similar winner-take-all strategy as in Buckner et al. [43] to 1,139 individuals from the original parcellation dataset (i.e., GSP). This resulted in a parcellation broadly consistent with known functional organization of the thalamus as well as published functional parcellations at the level of fMRI (e.g., [46, 48-50]; Fig. 3). This parcellation is publicly available at https://github.com/RaichleLab.

Intrinsic timescale estimation

To obtain a model-free estimate of intrinsic timescale while allowing for the exclusion of high-motion time points, we used a previously described approach for computing lagged (auto-) covariance using blocks of contiguous time points [31]. This method was applied to low-pass filtered time series (<0.1 Hz) [51], as fMRI SNR declines steeply above 0.1 Hz [52, 53].

The Pearson correlation coefficient, r, for zero-lag correlation between continuous signals, $x_1(t)$ and $x_2(t)$, is given by:

$$r_{x_1x_2} = \frac{1}{\sigma_{x_1}\sigma_{x_2}}\frac{1}{T}\int x_1(t)\cdot x_2(t)dt\,, \tag{1}$$

where σ_{x_1} and σ_{x_2} are the temporal standard deviations of the zero-mean signals x_1 and x_2 and T is the interval of integration. By generalizing this equation to accommodate temporal delays, τ, between the signals, correlation (or covariance, for simplicity) can be computed as a function of delay in seconds. Thus,

$$c_{x_1x_2}(\tau) = \frac{1}{T}\int x_1(t+\tau)\cdot x_2(t)dt \tag{2}$$

defines the cross-covariance function. In the special case $x_1 = x_2$, Eq. (2) defines the autocovariance function (ACF) $c_x(\tau)$.

In practice, we first construct the ACF in the time domain at discrete multiples of the TR (i.e., at the sampling interval) (see [31] for further detail). A single ACF for each session is obtained by summing unnormalized auto-covariance over blocks (b) of contiguous frames, and subsequently normalizing based on the total number of time points in a session contributing to a given ACF lag. Thus,

$$c_{x_b}(\Delta) = \sum_{t=1}^{N_b - \Delta} x_b(t+\Delta) \cdot x_b(t)\,, \tag{3}$$

$$c_x(\Delta) = \frac{1}{N_\Delta} \sum_{b=1}^{B} c_{x_b x_b}\,, \tag{4}$$

where Δ is the temporal shift in units of TRs, t indexes frames within the block, N_b is the total number of frames within the block, N_Δ is the total number of frames contributing to the ACF estimate at a particular temporal shift, and B is the total number of blocks. Time series are set to zero-mean prior to Equation (4) by subtracting the mean computed over the maximum number of realizations (i.e., all non-censored frames from the time series). Finally, $c_x(\Delta)$ is normalized by $c_x(0)$ to yield autocorrelation (rather than autocovariance), such that $c_x(0) = 1$.

$c_x(\Delta)$ was computed over Δ ∈ [-4, 4] in the GSP dataset (TR = 3.0 s) and Δ ∈ [-6, 6] in the MSC dataset (TR = 2.2 s). Performing minimal time shifts reduces the minimum duration required for a block of contiguous frames to contribute to each point of the ACF, which maximizes data usage [31]. Finally, the precise abscissa corresponding to $c_x = .5$ (i.e., half of the ACF FWHM) was estimated by computing the zeros of a spline fit to the ACF using the MATLAB "fnzeros" function [54]. Custom MATLAB code for intrinsic timescale estimation as described in this paper is publicly available at https://github.com/RaichleLab/lag-code.

For power spectra presented in Figure S1, Welch's power spectral density estimate was computed for each cortical vertex and averaged within each of the six networks across all 10 30-minute sessions from low-motion MSC subjects 1-6. Power spectra in Figure S1A were computed prior to denoising (i.e., following frame alignment and detrending but prior to any censoring, filtering or regression) while spectra in S1B were computed after the full denoising procedure described above. For computing spectra in S2B only, censored frames (i.e., framewise displacement >0.5 mm) were linearly interpolated.

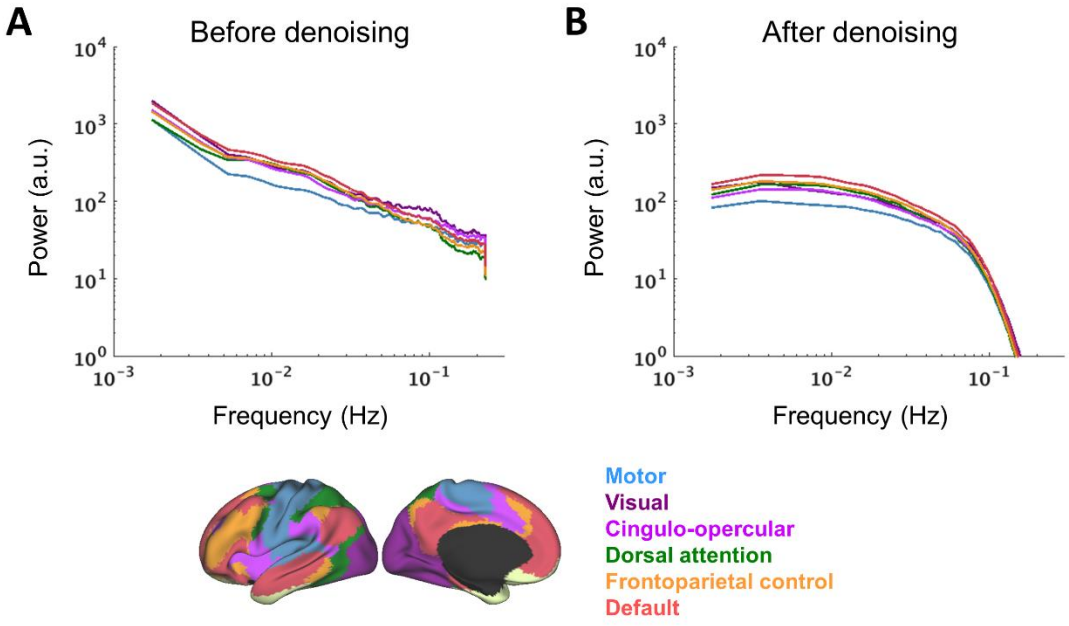

Fig. S1. Power spectral density of rsfMRI time series across the cortex. Mean group-averaged power spectra for each canonical network **(A)** before and **(B)** after denoising (see SI Methods). Spectra are not normalized by total power (variance). Note that regression leads to a flattening of lower frequencies in the absence of explicit high-pass filtering.

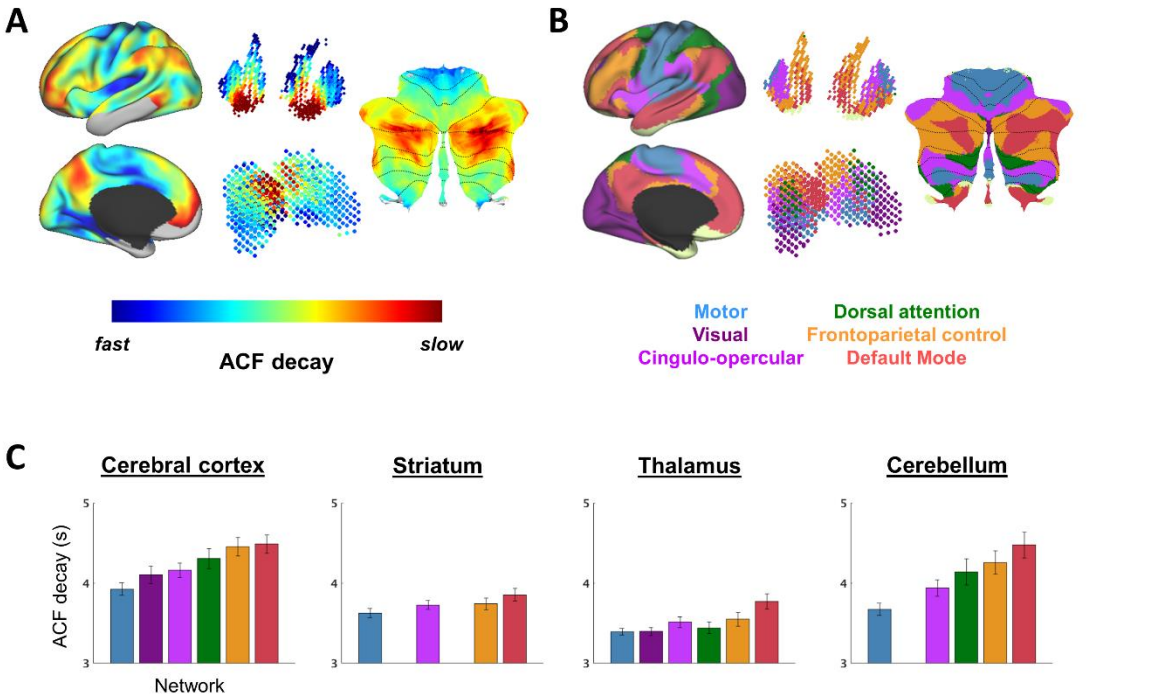

Fig. S2. Cortical and subcortical timescale organization in secondary dataset. (A) Intrinsic timescale computed for cortical and non-neocortical structures, including striatum and thalamus (middle) and cerebellum (right) (separate scale used for each structure), as in Fig. 2, but in the secondary dataset (see main text Methods). **(B)** Canonical large-scale functional networks as defined by Buckner et al. [42-44] (see main text Methods). **(C)** Mean intrinsic timescale (ACF decay) computed within each network for each brain structure analyzed. Mean and standard error (error bars) computed across subjects (N = 10).

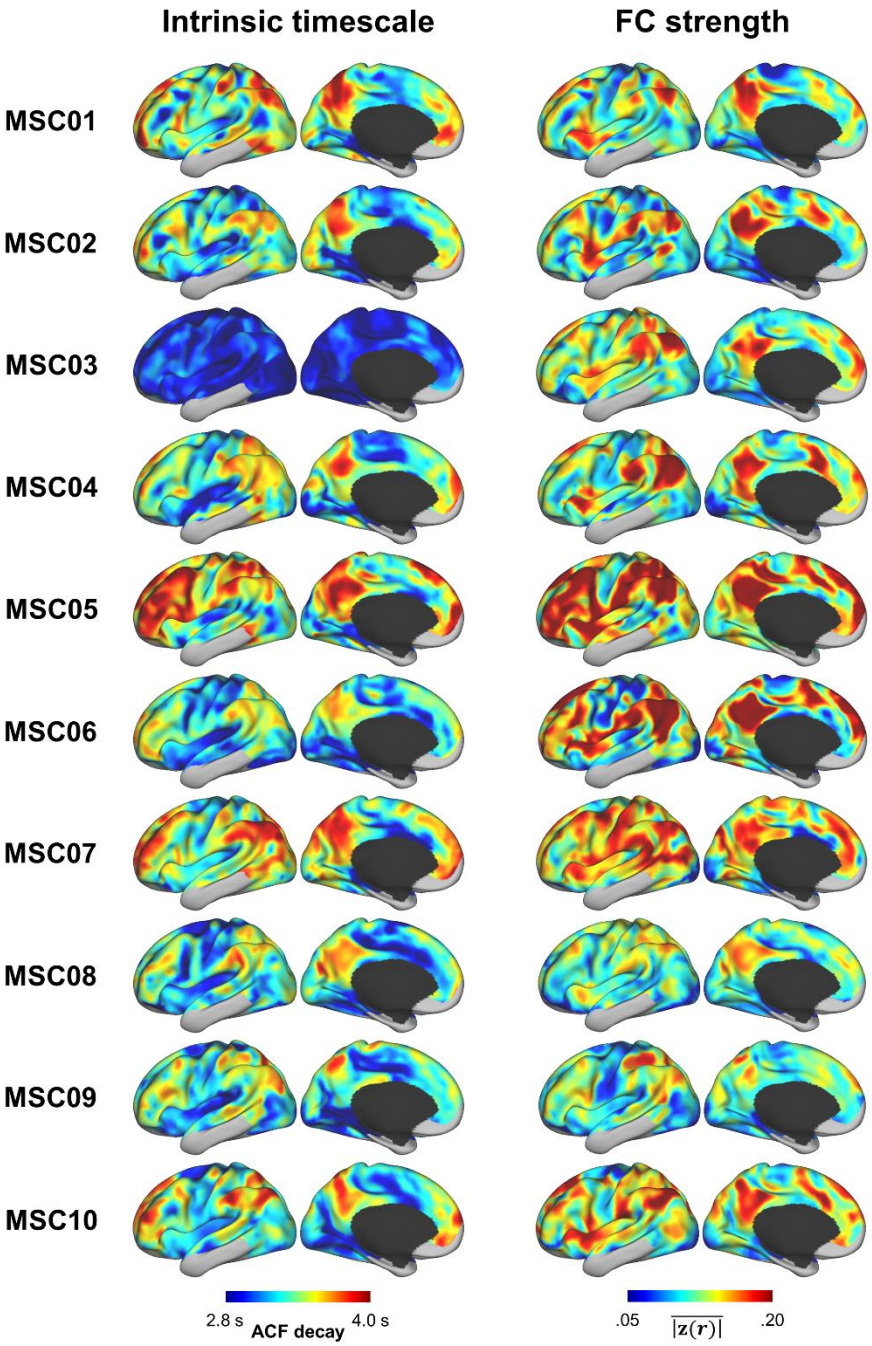

Fig. S3. Individual cortical maps of intrinsic timescale and FC strength. For each MSC subject, intrinsic timescale and FC strength were quantified by ACF decay and mean FC magnitude, respectively (see main text Methods). Subject-wise spatial correlations between these measures are presented in Fig. 4B.

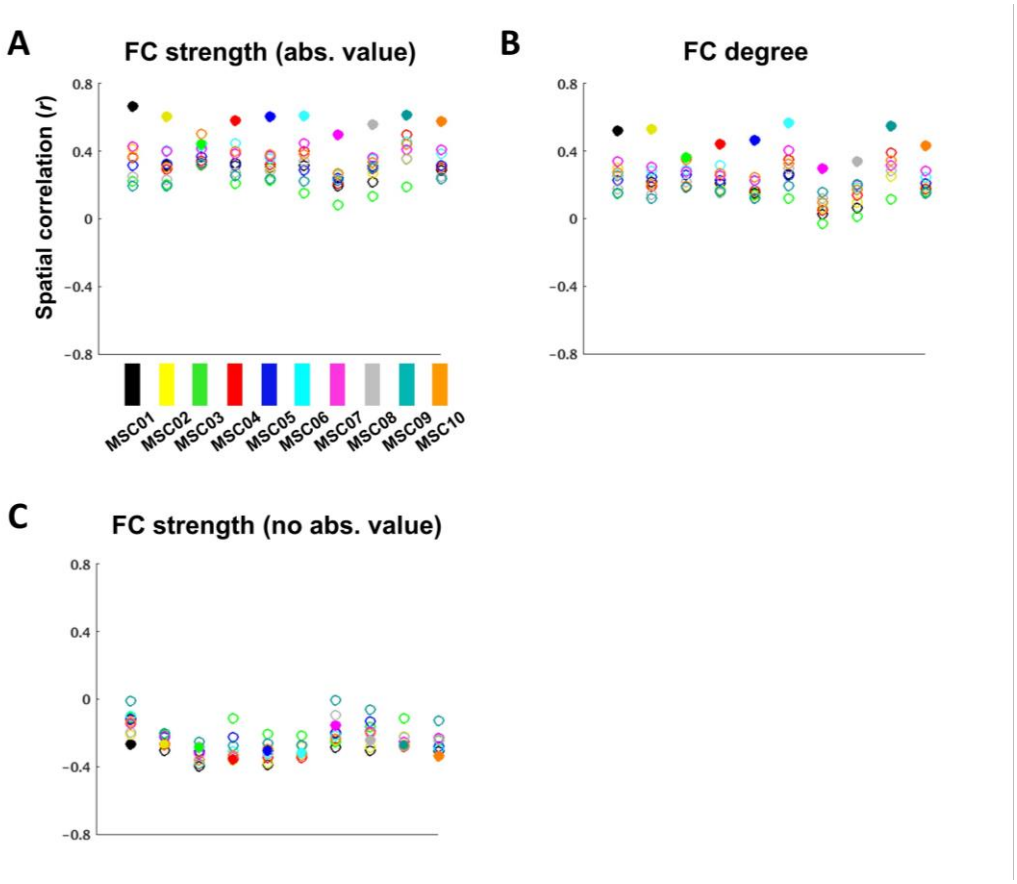

Fig. S4. Intrinsic timescale:FC relationships using different measures of FC. (A) Intrinsic timescale:FC relationships, where FC is quantified as mean absolute value FC strength (same as main text Fig. 4). **(B)** Same as (A), but with FC quantified as degree (number of correlations > +0.3). **(C)** Same as (A), but with FC quantified as mean non-absolute value FC strength. Thus, equal treatment of positive and negative correlations (A) or analysis of only strong positive correlations (B) yield results consistent with theoretical predictions and indicate individual specificity; allowing positive and negative correlations to cancel out (C) does not. See Supplementary Appendix, “Quantifying extensive functional connectivity” for further information.

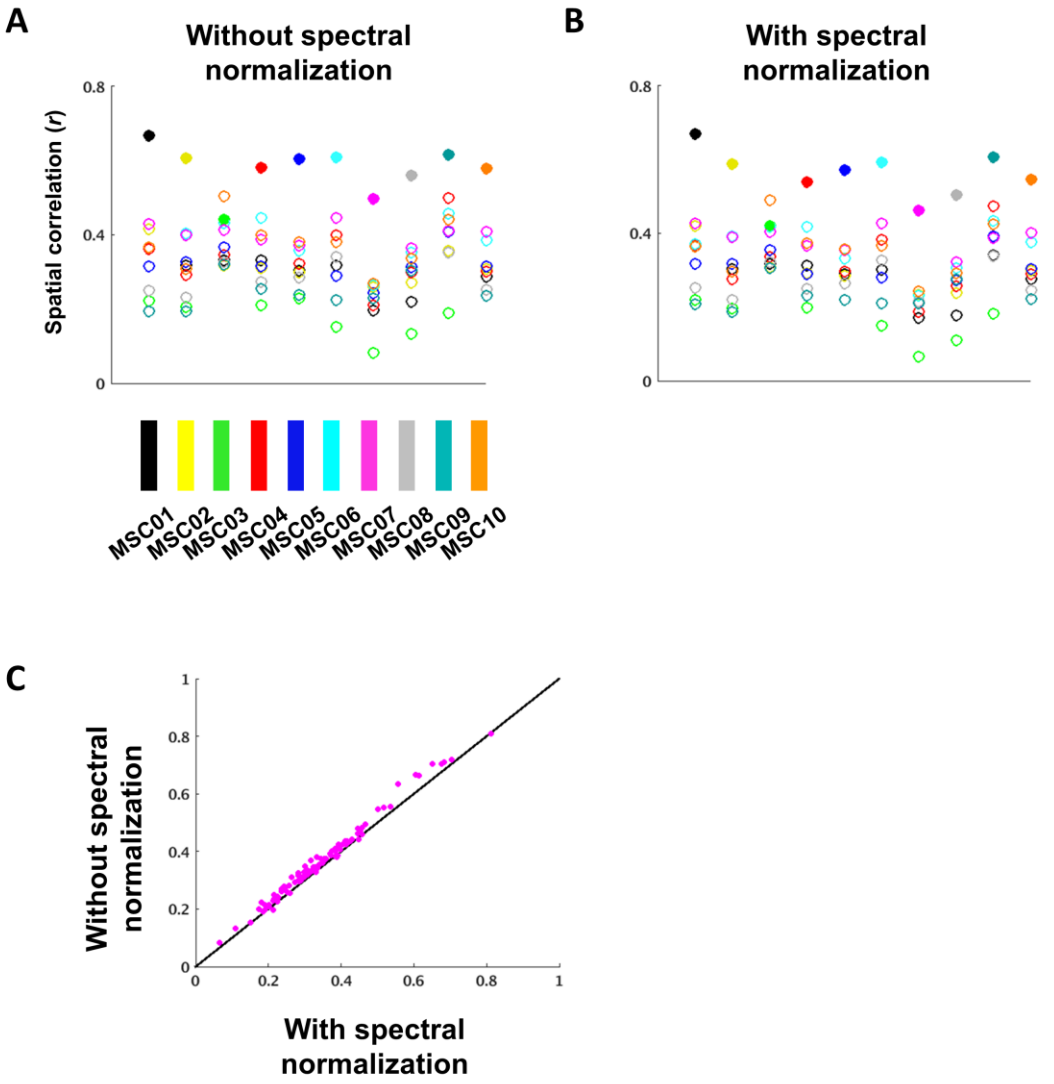

Fig. S5. Relationship between intrinsic timescale and FC strength after accounting for spectral variability. (A) Correlations between intrinsic timescale and FC strength, as in Fig. 4B. **(B)** Correlations between intrinsic timescale and FC strength following spectral normalization (see main text Methods). **(C)** Scatter plot depicting correlation values (i.e., all 100 *r* values between each individual's intrinsic timescale and FC strength maps) before and after spectral normalization. As expected, spectral normalization decreases correlations overall; however, changes are minimal. Hence, spectral variability does not materially contribute to the relationship between intrinsic timescale and FC strength in Fig. 4B.

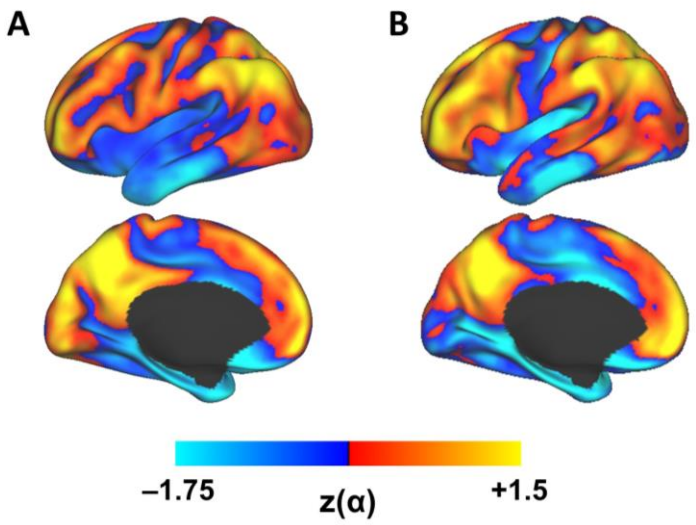

Fig. S6. Comparison with a previously published cortex-wide map of fMRI spectral content. **(A)** MSC group-averaged spectral content estimated as in [10] (compare with their Fig. 1B). Thus, for each vertex, spectral content was estimated as the slope (α) of the log-linear representation of the power spectrum from 0.01 to 0.2 Hz (fit by least-squares regression). α maps were computed for each individual (after averaging power spectra over all 10 sessions), Z-scored, and averaged across all 10 individuals. **(B)** Same as in (A), but with log-linear fit restricted to 0.01 to 0.1 Hz. Excluding frequencies above 0.1 Hz yields greater correspondence with results of the present study (main text, Fig. 1).

SI References

1. Rubinov, M. and O. Sporns, *Complex network measures of brain connectivity: uses and interpretations.* Neuroimage, 2010. **52**(3): p. 1059-69.
2. Power, J.D., et al., *Sources and implications of whole-brain fMRI signals in humans.* Neuroimage, 2017. **146**: p. 609-625.
3. Fox, M.D., et al., *The global signal and observed anticorrelated resting state brain networks.* J Neurophysiol, 2009. **101**(6): p. 3270-83.
4. Fox, M.D., et al., *The human brain is intrinsically organized into dynamic, anticorrelated functional networks.* Proc Natl Acad Sci U S A, 2005. **102**(27): p. 9673-8.
5. Shulman, G.L., et al., *Common Blood Flow Changes across Visual Tasks: II. Decreases in Cerebral Cortex.* J Cogn Neurosci, 1997. **9**(5): p. 648-63.
6. Raichle, M.E. and A.Z. Snyder, *A default mode of brain function: a brief history of an evolving idea.* Neuroimage, 2007. **37**(4): p. 1083-90; discussion 1097-9.
7. Keller, C.J., et al., *Neurophysiological investigation of spontaneous correlated and anticorrelated fluctuations of the BOLD signal.* J Neurosci, 2013. **33**(15): p. 6333-42.
8. Chen, A.C., et al., *Causal interactions between fronto-parietal central executive and default-mode networks in humans.* Proc Natl Acad Sci U S A, 2013. **110**(49): p. 19944-9.
9. Buckner, R.L., et al., *Cortical hubs revealed by intrinsic functional connectivity: mapping, assessment of stability, and relation to Alzheimer's disease.* J Neurosci, 2009. **29**(6): p. 1860-73.
10. Baria, A.T., et al., *Linking human brain local activity fluctuations to structural and functional network architectures.* Neuroimage, 2013. **73**: p. 144-55.
11. Chaudhuri, R., et al., *A Large-Scale Circuit Mechanism for Hierarchical Dynamical Processing in the Primate Cortex.* Neuron, 2015. **88**(2): p. 419-31.
12. Scholtens, L.H., et al., *Linking macroscale graph analytical organization to microscale neuroarchitectonics in the macaque connectome.* J Neurosci, 2014. **34**(36): p. 12192-205.
13. Runyan, C.A., et al., *Distinct timescales of population coding across cortex.* Nature, 2017. **548**(7665): p. 92-96.
14. Wasmuht, D.F., et al., *Intrinsic neuronal dynamics predict distinct functional roles during working memory.* Nat Commun, 2018. **9**(1): p. 3499.
15. Preller, K.H., et al., *Changes in global and thalamic brain connectivity in LSD-induced altered states of consciousness are attributable to the 5-HT2A receptor.* Elife, 2018. **7**.
16. Yang, G.J., et al., *Functional hierarchy underlies preferential connectivity disturbances in schizophrenia.* Proc Natl Acad Sci U S A, 2016. **113**(2): p. E219-28.
17. Demirtaş, M., et al., *Hierarchical Heterogeneity across Human Cortex Shapes Large-Scale Neural Dynamics.* Neuron, 2019. **101**(6): p. 1181-1194.e13.
18. Cole, M.W., S. Pathak, and W. Schneider, *Identifying the brain's most globally connected regions.* Neuroimage, 2010. **49**(4): p. 3132-48.
19. van den Heuvel, M.P. and O. Sporns, *Network hubs in the human brain.* Trends Cogn Sci, 2013. **17**(12): p. 683-96.
20. Laumann, T.O., et al., *Functional System and Areal Organization of a Highly Sampled Individual Human Brain.* Neuron, 2015. **87**(3): p. 657-70.
21. Talairach, J. and P. Tournoux, *"Co-planar stereotaxic atlas of the human brain."*. 1988, Thieme Medical Publishers, New York.
22. Power, J.D., et al., *Spurious but systematic correlations in functional connectivity MRI networks arise from subject motion.* Neuroimage, 2012. **59**(3): p. 2142-54.
23. Gordon, E.M., et al., *Precision Functional Mapping of Individual Human Brains.* Neuron, 2017. **95**(4): p. 791-807.e7.
24. Siegel, J.S., et al., *Data Quality Influences Observed Links Between Functional Connectivity and Behavior.* Cereb Cortex, 2017. **27**(9): p. 4492-4502.
25. Gratton, C., et al., *Removal of high frequency contamination from motion estimates in single-band fMRI saves data without biasing functional connectivity.* Neuroimage, 2020: p. 116866.

26. Carp, J., *Optimizing the order of operations for movement scrubbing: Comment on Power et al.* Neuroimage, 2013. **76**: p. 436-8.
27. Hallquist, M.N., K. Hwang, and B. Luna, *The nuisance of nuisance regression: spectral misspecification in a common approach to resting-state fMRI preprocessing reintroduces noise and obscures functional connectivity.* Neuroimage, 2013. **82**: p. 208-25.
28. Dale, A.M., B. Fischl, and M.I. Sereno, *Cortical surface-based analysis. I. Segmentation and surface reconstruction.* Neuroimage, 1999. **9**(2): p. 179-94.
29. Fischl, B., *FreeSurfer.* Neuroimage, 2012. **62**(2): p. 774-81.
30. Patriat, R., E.K. Molloy, and R.M. Birn, *Using Edge Voxel Information to Improve Motion Regression for rs-fMRI Connectivity Studies.* Brain Connect, 2015. **5**(9): p. 582-95.
31. Raut, R.V., et al., *On time delay estimation and sampling error in resting-state fMRI.* Neuroimage, 2019. **194**: p. 211-227.
32. Jenkinson, M., et al., *FSL.* Neuroimage, 2012. **62**(2): p. 782-90.
33. Dale, A.M. and M.I. Sereno, *Improved Localizadon of Cortical Activity by Combining EEG and MEG with MRI Cortical Surface Reconstruction: A Linear Approach.* J Cogn Neurosci, 1993. **5**(2): p. 162-76.
34. Fischl, B., M.I. Sereno, and A.M. Dale, *Cortical surface-based analysis. II: Inflation, flattening, and a surface-based coordinate system.* Neuroimage, 1999. **9**(2): p. 195-207.
35. Fischl, B., A. Liu, and A.M. Dale, *Automated manifold surgery: constructing geometrically accurate and topologically correct models of the human cerebral cortex.* IEEE Trans Med Imaging, 2001. **20**(1): p. 70-80.
36. Ségonne, F., et al., *A hybrid approach to the skull stripping problem in MRI.* Neuroimage, 2004. **22**(3): p. 1060-75.
37. Ségonne, F., E. Grimson, and B. Fischl, *A genetic algorithm for the topology correction of cortical surfaces.* Inf Process Med Imaging, 2005. **19**: p. 393-405.
38. Van Essen, D.C., et al., *Parcellations and hemispheric asymmetries of human cerebral cortex analyzed on surface-based atlases.* Cereb Cortex, 2012. **22**(10): p. 2241-62.
39. Van Essen, D.C., et al., *An integrated software suite for surface-based analyses of cerebral cortex.* J Am Med Inform Assoc, 2001. **8**(5): p. 443-59.
40. Marcus, D.S., et al., *Informatics and data mining tools and strategies for the human connectome project.* Front Neuroinform, 2011. **5**: p. 4.
41. Glasser, M.F., et al., *The minimal preprocessing pipelines for the Human Connectome Project.* Neuroimage, 2013. **80**: p. 105-24.
42. Yeo, B.T., et al., *The organization of the human cerebral cortex estimated by intrinsic functional connectivity.* J Neurophysiol, 2011. **106**(3): p. 1125-65.
43. Buckner, R.L., et al., *The organization of the human cerebellum estimated by intrinsic functional connectivity.* J Neurophysiol, 2011. **106**(5): p. 2322-45.
44. Choi, E.Y., B.T. Yeo, and R.L. Buckner, *The organization of the human striatum estimated by intrinsic functional connectivity.* J Neurophysiol, 2012. **108**(8): p. 2242-63.
45. Ojemann, J.G., et al., *Anatomic localization and quantitative analysis of gradient refocused echo-planar fMRI susceptibility artifacts.* Neuroimage, 1997. **6**(3): p. 156-67.
46. Greene, D.J., et al., *Integrative and Network-Specific Connectivity of the Basal Ganglia and Thalamus Defined in Individuals.* Neuron, 2019.
47. Marek, S., et al., *Spatial and Temporal Organization of the Individual Human Cerebellum.* Neuron, 2018. **100**(4): p. 977-993.e7.
48. Seitzman, B.A., et al., *A set of functionally-defined brain regions with improved representation of the subcortex and cerebellum.* Neuroimage, 2020. **206**: p. 116290.
49. Zhang, D., et al., *Noninvasive functional and structural connectivity mapping of the human thalamocortical system.* Cereb Cortex, 2010. **20**(5): p. 1187-94.
50. Hwang, K., et al., *The Human Thalamus Is an Integrative Hub for Functional Brain Networks.* J Neurosci, 2017. **37**(23): p. 5594-5607.
51. He, B.J., *Scale-free properties of the functional magnetic resonance imaging signal during rest and task.* J Neurosci, 2011. **31**(39): p. 13786-95.
52. Hathout, G.M., et al., *The lag of cerebral hemodynamics with rapidly alternating periodic stimulation: modeling for functional MRI.* Magn Reson Imaging, 1999. **17**(1): p. 9-20.

53. Anderson, J.S., *Origin of synchronized low-frequency blood oxygen level-dependent fluctuations in the primary visual cortex.* AJNR Am J Neuroradiol, 2008. **29**(9): p. 1722-9.
54. Mørken, K. and M. Reimers, *An unconditionally convergent method for computing zeros of splines and polynomials.* Mathematics of Computation, 2007. **76**(258): p. 845-865.